

Optimizing the geometry of aerodynamic lens injectors for single-particle coherent diffractive imaging of gold nanoparticles

Lena Worbs,^{1,2} Nils Roth,^{1,2} Jannik Lübke,^{1,2,3} Armando D. Estillore,¹
P. Lourdu Xavier,^{1,4} Amit K. Samanta,¹ and Jochen Kupper^{1,2,3,*}

¹Center for Free-Electron Laser Science, Deutsches Elektronen-Synchrotron DESY, Notkestraße 85, 22607 Hamburg, Germany

²Department of Physics, Universität Hamburg, Luruper Chaussee 149, 22761 Hamburg, Germany

³Center for Ultrafast Imaging, Universität Hamburg, Luruper Chaussee 149, 22761 Hamburg, Germany

⁴Max Planck Institute for the Structure and Dynamics of Matter, Luruper Chaussee 149, 22761 Hamburg, Germany

Single-particle x-ray diffractive imaging (SPI) of small (bio-)nanoparticles (NPs) requires optimized injectors to collect sufficient diffraction patterns to reconstruct the NP structure with high resolution. Typically, aerodynamic-lens-stack injectors are used for single NP injection. However, current injectors were developed for larger NPs ($\gg 100$ nm) and their ability to generate high-density NP beams suffers with decreasing NP size. Here, an aerodynamic-lens-stack injector with variable geometry and the geometry-optimization procedure are presented. The optimization for 50 nm gold NP (AuNP) injection using a numerical simulation infrastructure capable of calculating the carrier gas flow and the particle trajectories through the injector is introduced. The simulations are experimentally validated using spherical AuNPs and sucrose NPs. In addition, the optimized injector is compared to the standard-installation “Uppsala-injector” for AuNPs and results for these heavy particles show a shift in the particle-beam focus position rather than a change in beam size, which results in a lower gas background for the optimized injector. Optimized aerodynamic-lens stack injectors will allow to increase NP beam density, reduce the gas background, discover the limits of current injectors, and contribute to structure determination of small NPs using SPI.

I. INTRODUCTION

Simulations predicted the possibility of deriving high-resolution structures of biological macromolecules using x-ray free-electron lasers (XFELs) [1]. The ultra-short and extremely bright pulses of coherent x-rays provided by free-electron lasers (FELs) can outrun radiation damage processes before the particle has time to structurally respond and eventually be destroyed by the deposited energy [2]. Thus, the single-particle diffractive imaging (SPI) method at XFELs can be used to elucidate the structure of biological molecules [3, 4] without the need of highly ordered crystalline sample. SPI allows to retrieve the three-dimensional (3D) structure of biomolecules by reconstruction from a large number of two dimensional diffraction patterns, assembled into a 3D diffraction volume, requiring a high probability of an x-ray pulse interacting with an injected particle [5]. High-density particle-beams with ideally one particle per pulse and focus volume are generated to use both, x-rays and sample, efficiently. However, for the atomic resolution, ~ 100 pm, reconstruction of a protein, 10^5 to 10^6 diffraction patterns need to be collected [6].

Delivery of high-density single-particle-beams was demonstrated using aerodynamic-lens stacks (ALS) to generate focused beams of aerosolized particles from ambient conditions into vacuum [3, 5]. An ALS contains sets of thin apertures to manipulate the particles’ lateral spatial distribution before it exits through the last aperture into vacuum. Aerodynamic lenses enable successive

contractions of a flowing particle-beam and provide focusing to high particle-densities for wide range of particle sizes [7, 8]. Before adaption for SPI, they were mainly used in aerosol mass spectrometry to ensure a high transmission for a large particle size range [9]. A widely used ALS for SPI, readily available at many XFELs, is the so-called “Uppsala injector” (TSI model AFL100), which can deliver collimated or focused beams for a range of particle sizes, e. g., 0.1–300 μm [10]. It was successfully used in various experiments at XFEL facilities [10–13]. A recent experiment we performed at EuXFEL showed the successful collection of more than 10 million diffraction patterns from single gold nanoparticles using this injector and shows the opportunities provided by careful sample preparation and injection [5].

However, currently sample injection and beam formation is the bottleneck of collecting large data sets of small bio-particle diffraction patterns and injection schemes have to be modified accordingly [14]. The geometry of the “Uppsala injector” is fixed by design and the only tunable parameter to change the particle-beam focus size and position is the inlet pressure before the ALS [15]. To circumvent the increase of inlet pressure to generate a smaller particle-beam focus and thus an increase of pressure in the experimental chamber, we designed and used a new particle injector with variable geometry, as shown in Fig. 1, i. e., the inner tube diameter and the aperture diameter can be changed [16, 17] to produce the highest particle-beam density for a given particle size. In addition, the speed of the particles is important in SPI experiments. It should be as slow as possible to increase the particle-beam density and thus hitrate, but with increasing repetition rates at XFEL facilities the particle speed has to be sufficiently fast to avoid interaction of

* jochen.kuepper@cfel.de;

<https://www.controlled-molecule-imaging.org>

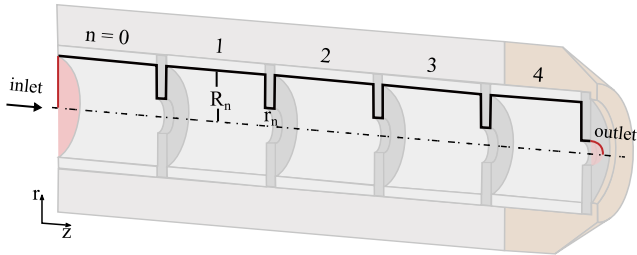


FIG. 1. Schematic of the ALS geometry, which is cylindrically symmetric about the dashed line. Carrier gas flows from left to right. The black solid line is the 2D geometry used for the simulations, consisting of five aperture and tube pieces. The inner radius (R_n) of the tube as well as the lens aperture radius (r_n) can be changed individually [17]; see text for details.

NPs with two x-ray pulses. For the full repetition rate of 4.5 MHz at EuXFEL [18] and an x-ray focus size of 2 μm , the particle speed has to exceed 10 m/s to enter the interaction region without interacting with the previous pulse, which can damage or scatter off the sample already.

Here, we present the geometry optimization for aerosolized spherical gold nanoparticles (AuNPs) of 50 nm diameter at typical inlet conditions for SPI experiments. The size is chosen as an intermediate step from large NPs and viruses (> 100 nm) towards single proteins (< 10 nm). The numerical simulation infrastructure used is presented elsewhere [16, 19]. To validate our simulation results, we compare them with experimental data for both AuNPs and sucrose spheres. AuNPs, when synthesized and prepared well, show a narrow size distribution similar to bio-particles and are therefore good benchmark samples for sizing and focusing experiments. AuNPs have a high scattering power resulting in good detection efficiencies both in x-ray scattering and for in-laboratory detection methods [20, 21]. Furthermore, AuNPs exhibit distinct physical and chemical properties with potential applications ranging from quantum electronics to biomedicine and potential drug delivery systems [22, 23]. Sucrose particles are often used at XFEL facilities for alignment in commissioning and startup experiments [11, 12], as the number density of the generated sucrose spheres is high and the particle-beam can be observed easily while aligning the injector to the x-ray beam. Most importantly, the mass density of sucrose NPs, and thus their focusing behavior, is comparable to biological matter, rendering them a good prototypical benchmark system for bio-nanoparticles.

II. METHODS

A. Geometry Optimization

Simulations of the ALS were performed as follows: First, we calculated the flow field of the carrier gas inside a

given 2D cylindrically symmetric geometry using a finite-element solver for the Navier-Stokes equations [24]. The flow field was calculated within the ALS geometry and extended after the exit with a quarter-circle with the radius of the last aperture serving as gas-expansion region of the vacuum chamber as shown in Fig. 1. The carrier gas was assumed to be nitrogen, as the particles were aerosolized using electrospray ionization (ESI), where the used gas mixture consists of ≈ 90 % nitrogen and ≈ 10 % CO_2 . As boundary conditions for the flow field we used mass-flow conservation of 13 mg/min as inlet condition and a pressure of 10^{-4} mbar at the end of the flow field along the semi-circle. Additional flow field calculations were performed using the inlet pressure as a boundary condition. Second, the trajectories of 100,000 particles for a given flow field were calculated with a homebuilt Python particle-tracing code [16]. Particles were introduced into the flow field with a uniform radial distribution covering the diameter of the first tube piece. We assumed the particles' velocity to be equal to the flow field values. We simulated trajectories of 50 nm diameter spherical particles with a density of 19.32 g/cm³, corresponding to the bulk density of gold. Transmitted particles were propagated further with their terminal speeds at the border of the flow field. Then, we determined the width of the resulting particle-beam depending on the distance from the ALS exit, i. e., the last aperture. Beam widths d_{70} were specified as the diameter where 70 % of the particles were in; d_{70} is a useful and robust metric as it is independent of the actual beam shape. Nevertheless, outside of the ALS all simulated particle-beams showed a peak-like radial distribution with the maximum of the particle density in the center ($r = 0$ mm).

The ALS consists of $n = 5$ aperture/tube pieces stacked onto another, see Fig. 1. The lens aperture radius r_n and the inner tube radius R_n can easily be adjusted. In our ALS, the aperture radius can be chosen from 0.75 mm to 5 mm in 0.25 mm steps. The lens apertures are interchangeable. The inner tube diameter could be chosen from parts with radius 2, 3, 4, 5, 6, 7.5, 8, 10 mm, which were available in stock; in principle, any size is possible. The inner diameter of the tubes is adjusted by adding an additional tube into the standard 10 mm diameter pieces.

As the variety corresponds to more than 7×10^{10} combinations we approached the optimization as follows: Our optimization procedure was performed iteratively from the exit to the entrance of the ALS, as the last aperture radius (r_4) largely determines the focus position and size of the particle beam. A larger r_4 aperture moves the particle-beam focus further outside or creates a collimated particle-beam and a smaller r_4 creates a particle-beam focus closer to the aperture or an even diverging particle-beam. We started the optimization in the last piece of the ALS, r_4 and R_4 . The particles were introduced into the flow field with a uniform radial distribution covering $r_{\text{initial}} = 0.02$ mm, mimicking that the lenses before already prefocused the particle-beam. The initial particle

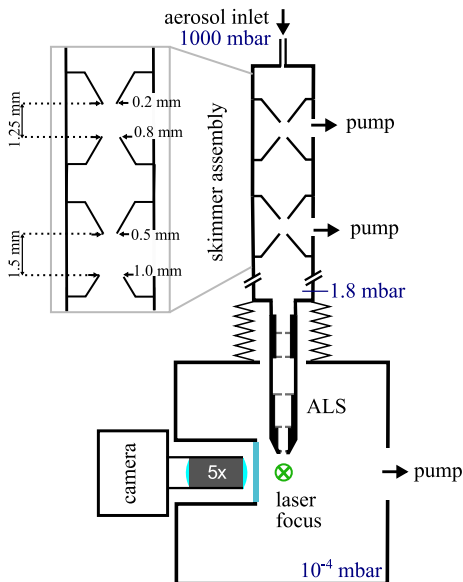


FIG. 2. Schematic of the experimental setup for the characterization of nanoparticle-beams. The aerosol passed a skimmer assembly to remove most of the carrier gas and the particles were focused using an ALS and entered the main vacuum chamber, where the particle-beam was crossed by a laser beam. The light scattered off the particles was collected using a camera-based microscope system [20, 21].

velocity was set equal to the flow fields speed. The best r_4 and R_4 combination fulfills the following condition: The transmission was $>90\%$, the focus was at $z > 4$ mm to suppress background scattering from the housing of the ALS, and it resulted in the smallest beam diameter. With this optimized r_4 and R_4 combination we then optimized r_3 and R_3 , and this was subsequently iterated for all lenses with increasing initial radial distribution of the particles, i. e., 0.02 mm for piece 4 and 3, 0.5 mm for piece 2, 1 mm for piece 1, and the whole radius of the lens filled before the first aperture. This optimization procedure reduces the efforts to 160 combinations per lens and <1000 overall.

B. Experimental Setup

We measured the particle-beam evolution of AuNPs from the optimized ALS geometry. The schematic of our experimental setup is shown in Fig. 2. It consists of four main parts: an aerosolization chamber, a differentially pumped transport tube, the ALS system for particle-beam formation, and the detection region for visualization of the particle-beam. To generate isolated test particles from the liquid sample, we injected spherical AuNPs with a diameter of (27 ± 2.25) nm in 5 mM ammonium acetate (AmAc) with a concentration of 10^{11} particles/ml and a 2 % sucrose solution in 20 mM AmAc using a commercial electro spray (TSI Advanced Electro spray 3482). The

aerosolized nanoparticles passed through a differentially pumped skimmer assembly for pressure reduction. The particles were focused into the detection chamber using the ALS. The pressure above the entrance of the the ALS was 1.8 mbar (Pfeiffer Vacuum CMR 361). In the main chamber, the pressure was kept at 2.5×10^{-4} mbar. The ALS is mounted on a motorized xyz -manipulator to perform height scans and measure the particle-beam evolution.

Particles were detected using a side-view illumination scheme [20]. A Nd:YAG laser (Innolas SpitLight, 532 nm, pulse duration 11.5 ns, pulse energy up to 240 mJ at 532 nm, 20 Hz repetition rate) was focused into the center of the vacuum chamber intersecting the particle-beam. The light scattered off the particles was collected using a camera-based microscope system [20, 21] consisting of a long working-distance objective (Edmund Optics, 5 \times magnification, numerical aperture $N_a = 0.14$, working distance $d = 34$ mm, depth of field 14 μm) and a high-efficiency sCMOS camera (Photometrics PrimeB95, quantum efficiency 0.95 at 532 nm, 1200×1200 pixels). This microscope yields a nominal resolution of 0.54 pixel/ μm . Images were collected with a 1 ms exposure time synchronized to the laser at 20 Hz such that every frame covered one laser pulse. For every distance of the ALS and the laser, we recorded 10000 images for the AuNP sample and 2000 images for the sucrose sample. We determined the positions of the particles by analyzing the images using a centroiding algorithm based on Hessian blob-finding [25]. The particles' positions were converted into a 2D histogram, see Supplementary Information for details. The width of the particle beam is determined from the projection of the particle-beam onto the laser propagation axis. The beam diameter is shown as d_{70} .

III. RESULTS

A. Optimization and Simulation Results

The optimization process resulted in one final geometry which produced a particle beam to our specifications. The resulting optimized-lens-stack geometry is shown in Fig. 3. From entrance to exit, the lens tube radius and the aperture radius are first increasing, then decreasing. The smallest lens tube radius and aperture radius are located at the last lens piece. Values are given next to the geometry. The velocity-flow field for 13 mg/min mass flow and particle trajectories for 50 nm AuNPs at different inlet positions (black solid lines) are shown in Fig. 3, demonstrating a clear focusing effect of the ALS.

For this ALS geometry, the 50 nm AuNP beam focused at a distance of 5.8 mm from the ALS exit with a particle-beam width of of 33 μm (d_{70}). The particle-beam evolution for 13 mg/min mass flow is shown in Fig. 4 a as the cyan curve. The particle-beam evolution is shown as the beam width (d_{70}) depending on the distance z from the ALS exit. We simulated the focusing

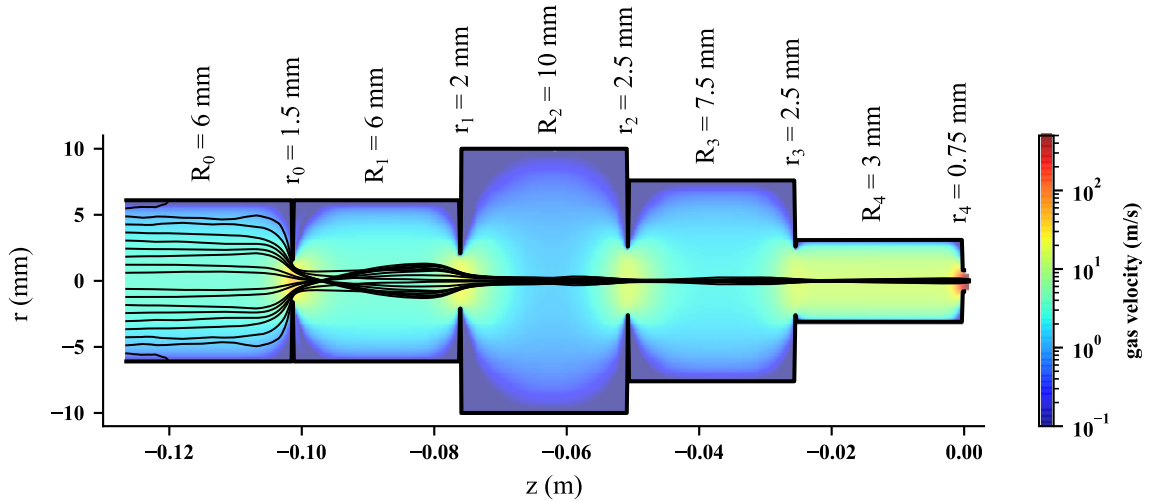


FIG. 3. Optimized ALS geometry. Tube and aperture radii are specified above the device and the corresponding nitrogen-gas flow-field for the injection of 50 nm AuNPs at 13 mg/min mass flow is depicted in false color. Representative (calculated) particle trajectories are shown by black lines, with gas and particle flow direction from left to right. A clear focusing effect of the different parts of the ALS can be observed through the radial narrowing of the set of particle trajectories.

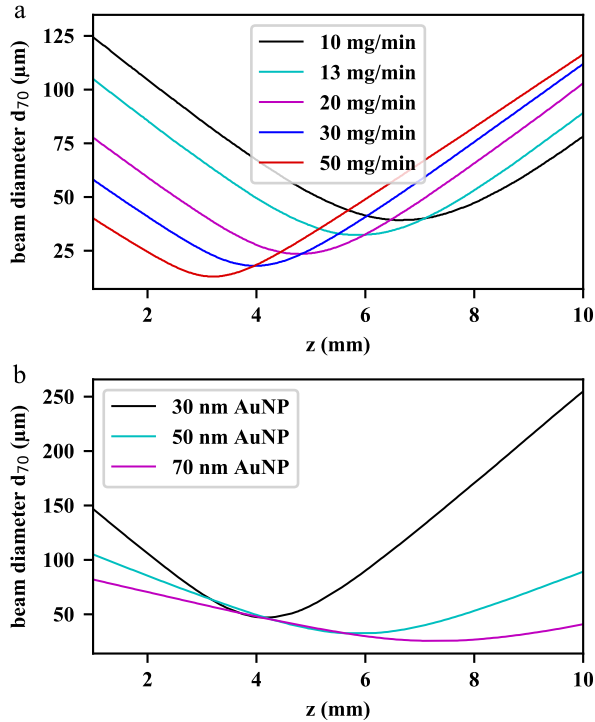


FIG. 4. (a) Particle-beam evolution curves of the optimized injector for 50 nm AuNPs at different gas-mass flows. The width of the particle-beam was determined as d_{70} . With increasing mass flow and thus pressure before the ALS, the particle-beam focus becomes harder, i. e., it moves closer to the ALS exit and gets smaller. (b) Particle-beam evolution curve of the optimized injector for different AuNP sizes at 13 mg/min mass flow. With increasing particle size, the particle-beam focus decreases and moves further away from the ALS. The convergence increases with decreasing particle size.

behavior for different mass flow conditions between 10 and 50 mg/min. With increasing mass flow, the focus shifted closer to the exit of the ALS and the focus size decreased. At 50 mg/min mass flow, the particle-beam focus size decreased to 13 μm at a distance of 3.2 mm. Similar behavior has been shown experimentally for the “Uppsala-injector” [15]. Therefore, working at higher mass flow is desired, but it will increase the amount of gas introduced into the interaction chamber and result in a higher pressure and thus a higher gas-scattering background in diffractive imaging experiments.

At 13 mg/min mass flow the AuNPs exiting from the optimized ALS had a mean velocity of 29 m/s. Mean velocities and beam diameter values for different flow conditions are given in the Supplementary Information. The behavior of the ALS optimized for 50 nm AuNPs was compared to smaller and larger diameters of the AuNPs as shown in Fig. 4 b. For smaller AuNPs the focus moved closer to the ALS and was larger, whereas bigger particles were focused further away and showed a smaller focus size. An interesting feature observed was the change of the convergence depending on the particle size: The smaller the particles were, the larger the convergence became. A precise positioning for small particles becomes necessary to meet the particle-beam focus. This change of the convergence is due to the larger momentum of larger particles interacting with the gas flow field.

B. Experimental Results

We measured particle-beam evolution curves of AuNPs and sucrose particles. The AuNP data with standard errors is shown in Fig. 5 a as beam diameter (d_{70}) de-

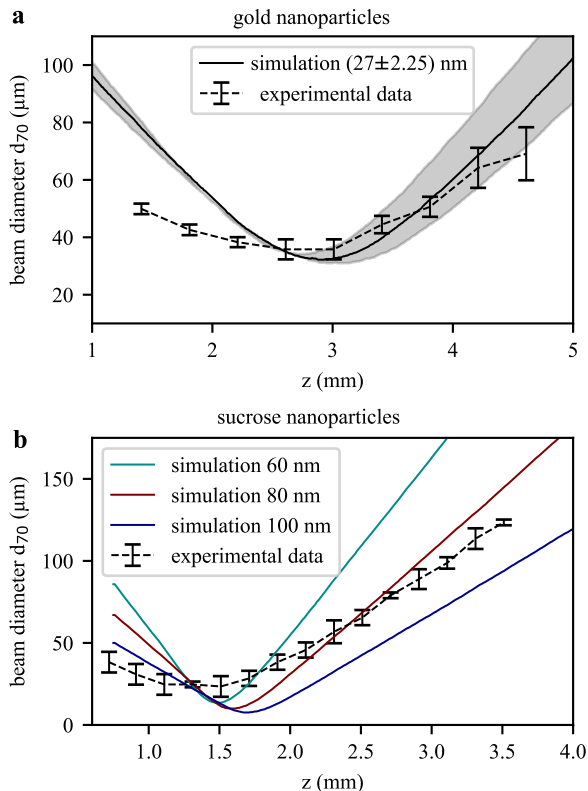


FIG. 5. (a) Experimental particle-beam size evolution for (27 ± 2.25) nm AuNPs (black dashed line). Simulated beam evolution is shown for 27 nm (black solid line) with the spread of the beam diameter due to the size distribution of ± 2.25 nm (grey area). (b) Experimental particle-beam size evolution for sucrose spheres (black). The experimental data agrees reasonably well with a simulated particle size of 80 nm (dark red).

pending on the distance from the injector exit, along with simulations for the particle size of (27 ± 2.25) nm using the experimentally measured inlet pressure of 1.8 mbar above the ALS. The experimental and simulated particle-beam diameters agree well, especially at and after the focus of the particle-beam. Some deviations are observed before the focus, where the simulation overestimates the beam diameter, e. g., by a factor of ~ 1.5 at $z = 1.4$ mm. However, the most relevant parameters for SPI experiments, the focus position and focus size, are in excellent agreement between experiment and simulation. The same experiment is repeated for a 2 % sucrose solution to generate spherical sucrose particles in the electrospray process with a broad size distribution around 80 nm, shown in the Supplementary Information. The sucrose-particle-beam evolution is shown in Fig. 5 b with standard errors (black) and compared to simulations for different sizes of sucrose spheres ($\rho = 1.59$ g/cm³). Overall, the experimental data is described well by the simulation for 80 nm sucrose spheres. Similar to the AuNP data, the simulation agrees well with our data after the focus, although before the focus the simulation deviates by a factor of ~ 1.6 at

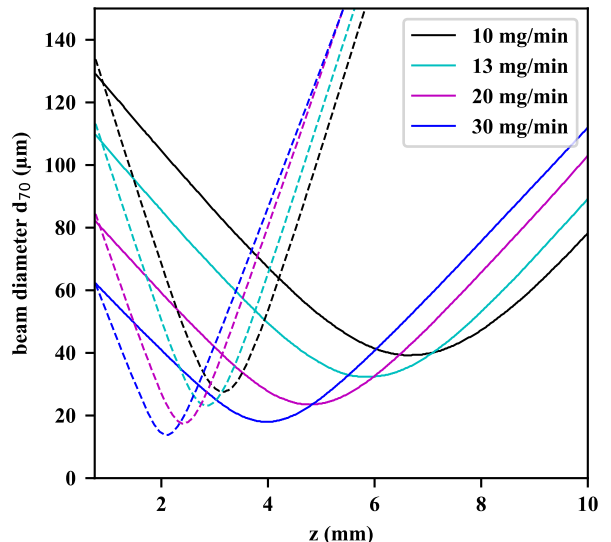


FIG. 6. Simulated particle-beam evolution curves of 50 nm AuNPs exiting from the “Uppsala-injector” (dashed lines) for different mass flow conditions in comparison to the corresponding focusing curves from our optimized injector (solid lines).

$z = 0.8$ mm. This mismatch is partly due to the broad experimental size distribution, i. e., the experimental data does not correspond to a single particle-size simulation.

C. “Uppsala-injector” simulation

The “Uppsala-injector” (AFL100) was introduced before and used in various experiments at XFELs [10–13]. We simulated its focusing of 50 nm AuNPs and compared it to our optimized ALS.

The beam evolution curves for 50 nm AuNPs at different mass flow conditions for this injector are shown in Fig. 6 (dashed lines), along with the focusing curves for our optimized injector (solid lines). The simulated transmission of 50 nm AuNPs through both injectors was above 90 %, i. e., at 13 mg/min mass flow the transmission was 91.9 % for the AFL100 and 93.4 % for our optimized injector. At the same mass flow the AFL100 showed slightly smaller mean velocities of the exiting particles than our optimized injector. As an example, at 13 mg/min mass flow, 50 nm AuNPs exiting the “Uppsala-injector” showed a mean velocity of 27 m/s. In comparison, particles in our injector reached a velocity of 29 m/s. A detailed list of velocities depending on mass flow is shown in the Supplementary Information.

IV. DISCUSSION

Our simulations show that the focus size is comparable for both injectors, but the difference is in the focus

position and the convergence. Our injector focuses the particles further downstream and the focusing is not as hard as for the AFL100. Generating a focused particle-beam further away from the injector exit has the advantage of a lower background from the nitrogen and CO₂ gas. Light gas diverges fast from the exit of the ALS into the vacuum chamber.

The focus position of the AFL100 is closer to the injector exit and can cause problems when using smaller particles and particles with lower sample density, such as bio-particles: The smaller and lighter the particles are the closer the focus position. As an example, we performed simulations for 10 nm AuNPs at 13 mg/min nitrogen mass flow for the AFL100 showing the focus position moves very close to the ALS exit, below $z = 1.5$ mm; the transmission is reduced to 59 %. Our 50 nm-optimized injector still shows a transmission of 79 % for those particles and a focus position above $z = 2$ mm; see Supplementary Information for details. The same behavior holds for the particle density: The lower the particle density (biomolecules), the closer the particle-beam focus becomes. For isolated proteins, it is almost impossible to focus the particle-beam with these injectors. In this case, an appropriate geometry optimization could result in a particle-beam focus further away from the injector exit.

V. CONCLUSION

We presented an optimization procedure of an ALS for 50 nm AuNPs using our previously developed computer-simulation framework for ALS injectors [16, 19] including the results of this optimization. We experimentally benchmarked the optimized geometry for beams of spherical gold and sucrose nanoparticles. Both particle-beam-evolution curves are in good agreement with the simulations. This validates our simulation framework, which can be used to get further insight into the fluid-dynamics focusing process and to develop optimized particle injectors for different sizes and materials, as well as for different

experimental conditions, such as inlet pressure and gas type.

We compared our optimized injector to the widely used AFL100 “Uppsala-injector” for 50 nm AuNPs. Both injectors create a focused particle-beam for different inlet mass flow conditions, and the main difference is observed in the particle-beam focus position, which for our optimized injector is further downstream, which reduces the carrier gas background at the focus and will be greatly beneficial for x-ray diffractive imaging, especially of small bio-particles that exhibit only small scattering signals.

Our variable injector geometry allows us to vary the particle-beam focus independent from the inlet pressure by varying the geometry and thus keeping the pressure after the injector, i. e., in the x-ray interaction region, constant. Generating high-quality particle-beams of nanoparticles does not only allow for structure determination by an increased number of collected diffraction patterns, but in addition it opens the field of time-resolved imaging of nanoparticle dynamics in future pump-probe-type experiments at XFELs.

ACKNOWLEDGEMENT

We thank Simon Welker for helpful discussions on improvements of the particle trajectory calculations. This work has been supported by the European Research Council under the European Union’s Seventh Framework Program (FP7/2007-2013) through the Consolidator Grant COMOTION (614507) and the Cluster of Excellence “Advanced Imaging of Matter” (AIM, EXC 2056, ID 390715994) of the Deutsche Forschungsgemeinschaft (DFG). Parts of this research were supported by the Maxwell computational resources operated at DESY. P. Lourdu Xavier acknowledges a fellowship from the Joachim Herz Stiftung.

-
- [1] R. Neutze, R. Wouts, D. van der Spoel, E. Weckert, and J. Hajdu, Potential for biomolecular imaging with femtosecond x-ray pulses, *Nature* **406**, 752 (2000).
- [2] H. N. Chapman, A. Barty, M. J. Bogan, S. Boutet, S. Frank, S. P. Hau-Riege, S. Marchesini, B. W. Woods, S. Bajt, W. H. Benner, L. W. A., E. Plönjes, M. Kuhlmann, R. Treusch, S. Düsterer, T. Tschentscher, J. R. Schneider, E. Spiller, T. Möller, C. Bostedt, M. Hoener, D. A. Shapiro, K. O. Hodgson, D. van der Spoel, F. Burmeister, M. Bergh, C. Caleman, G. Huldt, M. M. Seibert, F. R. N. C. Maia, R. W. Lee, A. Szöke, N. Timneanu, and J. Hajdu, Femtosecond diffractive imaging with a soft-x-ray free-electron laser, *Nat. Phys.* **2**, 839 (2006).
- [3] M. J. Bogan, W. H. Benner, S. Boutet, U. Rohner, M. Frank, A. Barty, M. M. Seibert, F. Maia, S. Marchesini, S. Bajt, B. Woods, V. Riot, S. P. Hau-Riege, M. Svenda, E. Marklund, E. Spiller, J. Hajdu, and H. N. Chapman, Single particle x-ray diffractive imaging, *Nano Lett.* **8**, 310 (2008).
- [4] A. Aquila, A. Barty, C. Bostedt, S. Boutet, G. Carini, D. DePonte, P. Drell, S. Doniach, K. H. Downing, T. Earnest, H. Elmlund, V. Elser, M. Gühr, J. Hajdu, J. Hastings, S. P. Hau-Riege, Z. Huang, E. E. Lattman, F. R. N. C. Maia, S. Marchesini, A. Ourmazd, C. Pellegrini, R. Santra, I. Schlichting, C. Schroer, J. C. H. Spence, I. A. Vartanyants, S. Wakatsuki, W. I. Weis, and G. J. Williams, The linac coherent light source single particle imaging road map, *Struct. Dyn.* **2**, 041701 (2015).
- [5] K. Ayyer, P. L. Xavier, J. Bielecki, Z. Shen, B. J. Daurer, A. K. Samanta, S. Awel, R. Bean, A. Barty, M. Bergemann, T. Ekeberg, A. D. Estillore, H. Fan-

- gohr, K. Giewekemeyer, M. S. Hunter, M. Karnevskiy, R. A. Kirian, H. Kirkwood, Y. Kim, J. Koliyadu, H. Lange, R. Letrun, J. Lübke, T. Michelat, A. J. Morgan, N. Roth, T. Sato, M. Sikorski, F. Schulz, J. C. H. Spence, P. Vagovic, T. Wollweber, L. Worbs, O. Yefanov, Y. Zhuang, F. R. N. C. Maia, D. A. Horke, J. Küpper, N. D. Loh, A. P. Mancuso, and H. N. Chapman, 3D diffractive imaging of nanoparticle ensembles using an x-ray laser, *Optica* **8**, 15 (2021), arXiv:2007.13597 [physics].
- [6] I. Poudyal, M. Schmidt, and P. Schwander, Single-particle imaging by x-ray free-electron lasers—how many snapshots are needed?, *Structural Dynamics* **7**, 024102 (2020), <https://doi.org/10.1063/1.5144516>.
- [7] M. J. Bogan, S. Boutet, H. N. Chapman, S. Marchesini, A. Barty, W. H. Benner, U. Rohner, M. Frank, S. P. Hau-Riege, S. Bajt, B. Woods, M. M. Seibert, B. Iwan, N. Timneanu, J. Hajdu, and J. Schulz, Aerosol imaging with a soft x-ray free electron laser, *Aerosol Sci. Techn.* **44**, i (2010).
- [8] W. H. Benner, M. J. Bogan, U. Rohner, S. Boutet, B. Woods, and M. Frank, Non-destructive characterization and alignment of aerodynamically focused particle beams using single particle charge detection, *J. Aerosol. Sci.* **39**, 917 (2008).
- [9] M. R. Canagaratna, J. T. Jayne, J. L. Jimenez, J. D. Allan, M. R. Alfarra, Q. Zhang, T. B. Onasch, F. Drewnick, H. Coe, A. Middlebrook, A. Delia, L. R. Williams, A. M. Trimborn, M. J. Northway, P. F. DeCarlo, C. E. Kolb, P. Davidovits, and D. R. Worsnop, Chemical and microphysical characterization of ambient aerosols with the aerodyne aerosol mass spectrometer, *Mass Spectrom. Rev.* **26**, 185 (2007).
- [10] M. F. Hantke, D. Hasse, M. R. N. C., T. Ekeberg, K. John, M. Svenda, N. D. Loh, A. V. Martin, N. Timneanu, L. S. D. van der SchotGijs, G. H. Carlsson, M. Ingelman, J. Andreasson, D. Westphal, M. Liang, F. Stellato, D. P. Deponte, R. Hartmann, N. Kimmel, R. A. Kirian, M. M. Seibert, K. Mühligh, S. Schorb, K. Ferguson, C. Bostedt, S. Carron, J. D. Bozek, D. Rolles, A. Rudenko, S. Epp, H. N. Chapman, A. Barty, J. Hajdu, and I. Andersson, High-throughput imaging of heterogeneous cell organelles with an x-ray laser, *Nat. Photon.* **8**, 943 (2014).
- [11] P. J. Ho, B. J. Daurer, M. F. Hantke, J. Bielecki, A. Al Haddad, M. Bucher, G. Doumy, K. R. Ferguson, L. Flückiger, T. Gorkhover, B. Iwan, C. Knight, S. Moeller, T. Osipov, D. Ray, S. H. Southworth, M. Svenda, N. Timneanu, A. Ulmer, P. Walter, J. Hajdu, L. Young, F. R. N. C. Maia, and C. Bostedt, The role of transient resonances for ultra-fast imaging of single sucrose nanoclusters, *Nature Communications* **11**, 167 (2020).
- [12] J. Bielecki, M. F. Hantke, B. J. Daurer, H. K. N. Reddy, D. Hasse, D. S. D. Larsson, L. H. Gunn, M. Svenda, A. Munke, J. A. Sellberg, L. Flueckiger, A. Pietrini, C. Nettelblad, I. Lundholm, G. Carlsson, K. Okamoto, N. Timneanu, D. Westphal, O. Kulyk, A. Higashiura, G. van der Schot, N.-T. D. Loh, T. E. Wysong, C. Bostedt, T. Gorkhover, B. Iwan, M. M. Seibert, T. Osipov, P. Walter, P. Hart, M. Bucher, A. Ulmer, D. Ray, G. Carini, K. R. Ferguson, I. Andersson, J. Andreasson, J. Hajdu, and F. R. N. C. Maia, Electrospray sample injection for single-particle imaging with x-ray lasers, *Science Advances* **5**, eaav8801 (2019).
- [13] M. M. Seibert, T. Ekeberg, F. R. N. C. Maia, M. Svenda, J. Andreasson, O. Jönsson, D. Odić, B. Iwan, A. Rocker, D. Westphal, M. Hantke, D. P. Deponte, A. Barty, J. Schulz, L. Gumprecht, N. Coppola, A. Aquila, M. Liang, T. A. White, A. Martin, C. Coleman, S. Stern, C. Abergel, V. Seltzer, J.-M. Claverie, C. Bostedt, J. D. Bozek, S. Boutet, A. A. Miahnahri, M. Messerschmidt, J. Krzywinski, G. Williams, K. O. Hodgson, M. J. Bogan, C. Y. Hampton, R. G. Sierra, D. Starodub, I. Andersson, S. Bajt, M. Barthelmess, J. C. H. Spence, P. Fromme, U. Weierstall, R. Kirian, M. Hunter, R. B. Doak, S. Marchesini, S. P. Hau-Riege, M. Frank, R. L. Shoeman, L. Lomb, S. W. Epp, R. Hartmann, D. Rolles, A. Rudenko, C. Schmidt, L. Foucar, N. Kimmel, P. Holl, B. Rudek, B. Erk, A. Hömke, C. Reich, D. Pietschner, G. Weidenpointner, L. Strüder, G. Hauser, H. Gorke, J. Ullrich, I. Schlichting, S. Herrmann, G. Schaller, F. Schopper, H. Soltau, K.-U. Kühnel, R. Andritschke, C.-D. Schröter, F. Krasniqi, M. Bott, S. Schorb, D. Rupp, M. Adolph, T. Gorkhover, H. Hirsemann, G. Potdevin, H. Graaf-sma, B. Nilsson, H. N. Chapman, and J. Hajdu, Single mimivirus particles intercepted and imaged with an X-ray laser, *Nature* **470**, 78 (2011).
- [14] J. Bielecki, F. R. N. C. Maia, and A. P. Mancuso, Perspectives on single particle imaging with x rays at the advent of high repetition rate x-ray free electron laser sources, *Structural Dynamics* **7**, 040901 (2020), <https://doi.org/10.1063/4.0000024>.
- [15] M. F. Hantke, J. Bielecki, O. Kulyk, D. Westphal, D. S. D. Larsson, M. Svenda, H. K. N. Reddy, R. A. Kirian, J. Andreasson, J. Hajdu, and F. R. N. C. Maia, Rayleigh-scattering microscopy for tracking and sizing nanoparticles in focused aerosol beams, *IUCrJ* **5**, 673 (2018).
- [16] N. Roth, S. Awel, D. A. Horke, and J. Küpper, Optimizing aerodynamic lenses for single-particle imaging, *J. Aerosol. Sci.* **124**, 17 (2018), arXiv:1712.01795 [physics].
- [17] N. Roth, D. Horke, J. Lübke, A. K. Samanta, A. Estillore, L. Worbs, N. Pohlman, K. Ayer, A. Morgan, H. Fleckenstein, M. Domaracky, B. Erk, C. Passow, J. Correa, O. Yefanov, A. Barty, M. Prasciolu, S. Bajt, R. Kirian, H. Chapman, and J. Küpper, New aerodynamic lens injector for single particle diffractive imaging, *Rev. Sci. Instrum.* (2021), submitted, arXiv:2012.11237 [physics].
- [18] W. Decking, S. Abeghyan, P. Abramian, A. Abramsky, A. Aguirre, C. Albrecht, P. Alou, M. Altarelli, P. Altmann, K. Amyan, V. Anashin, E. Apostolov, K. Appel, D. Auguste, V. Ayvazyan, S. Baark, F. Babies, N. Baboi, P. Bak, V. Balandin, R. Baldinger, B. Baranasic, S. Barbanotti, O. Belikov, V. Belokurov, L. Belova, V. Belyakov, S. Berry, M. Bertucci, B. Beutner, A. Block, M. Blöcher, T. Böckmann, C. Bohm, M. Böhnert, V. Bondar, E. Bondarchuk, M. Bonezzi, P. Borowiec, C. Bösch, U. Bösenberg, A. Bosotti, R. Böspflug, M. Bousonville, E. Boyd, Y. Bozhko, A. Brand, J. Branlard, S. Briechele, F. Brinker, S. Brinker, R. Brinkmann, S. Brockhauser, O. Brovko, H. Brück, A. Brüdgam, L. Butkowski, T. Büttner, J. Calero, E. Castro-Carballo, G. Cattalanotto, J. Charrier, J. Chen, A. Cherepenko, V. Cheskidov, M. Chiodini, A. Chong, S. Choroba, M. Chorowski, D. Churanov, W. Cichalewski, M. Clausen, W. Clement, C. Cloué, J. A. Cobos, N. Coppola, S. Cunis, K. Czuba, M. Czwalińska, B. D’Almagne, J. Dammann, H. Danared, A. de Zubiaurre Wagner, A. Delfs, T. Delfs, F. Dietrich, T. Dietrich, M. Dohls, M. Dommach, A. Donat,

- X. Dong, N. Doynikov, M. Dressel, M. Duda, P. Duda, H. Eckoldt, W. Ehsan, J. Eidam, F. Eints, C. Engling, U. Englisch, A. Ermakov, K. Escherich, J. Eschke, E. Saldin, M. Faesing, A. Fallou, M. Felber, M. Fenner, B. Fernandes, J. M. Fernández, S. Feucker, K. Filippakopoulos, K. Floettmann, V. Fogel, M. Fontaine, A. Francés, I. F. Martin, W. Freund, T. Freyermuth, M. Friedland, L. Fröhlich, M. Fusetti, J. Fydrych, A. Galas, O. García, L. Garcia-Tabares, G. Geloni, N. Gerasimova, C. Gerth, P. Geßler, V. Gharibyan, M. Gloor, J. Głowinkowski, A. Goessel, Z. Gołębiewski, N. Golubeva, W. Grabowski, W. Graeff, A. Grebentsov, M. Grecki, T. Grevsmuehl, M. Gross, U. Grosse-Wortmann, J. Grünert, S. Grunewald, P. Grzegory, G. Feng, H. Guler, G. Gusev, J. L. Gutierrez, L. Hagge, M. Hamberg, R. Hanneken, E. Harms, I. Hartl, A. Hauberg, S. Hauf, J. Hauschildt, J. Hauser, J. Havlicek, A. Hedqvist, N. Heidbrook, F. Hellberg, D. Henning, O. Hensler, T. Hermann, A. Hidvégi, M. Hierholzer, H. Hintz, F. Hoffmann, M. Hoffmann, M. Hoffmann, Y. Holler, M. Hüning, A. Ignatenko, M. Ilchen, A. Iluk, J. Iversen, M. Izquierdo, L. Jachmann, N. Jardon, U. Jastrow, K. Jensch, J. Jensen, M. Jeżabek, M. Jidda, H. Jin, N. Johansson, R. Jonas, W. Kaabi, D. Kaefer, R. Kammering, H. Kapitza, S. Karabekyan, S. Karstensen, K. Kasprzak, V. Katalev, D. Keese, B. Keil, M. Kholopov, M. Killenberger, B. Kitaev, Y. Klimchenko, R. Klos, L. Knebel, A. Koch, M. Koepke, S. Köhler, W. Köhler, N. Kohlstrunk, Z. Konopkova, A. Konstantinov, W. Kook, W. Koprek, M. Körfer, O. Korth, A. Kosarev, K. Kosiński, D. Kostin, Y. Kot, A. Kotarba, T. Kozak, V. Kozak, R. Kramert, M. Krasilnikov, A. Krasnov, B. Krause, L. Kravchuk, O. Krebs, R. Kretschmer, J. Kreutzkamp, O. Kröplin, K. Krzysik, G. Kube, H. Kuehn, N. Kujala, V. Kulikov, V. Kuzminych, D. La Civita, M. Lacroix, T. Lamb, A. Lancetov, M. Larsson, D. Le Pinvidic, S. Lederer, T. Lensch, D. Lenz, A. Leuschner, F. Levenhagen, Y. Li, J. Liebing, L. Lilje, T. Limberg, D. Lipka, B. List, J. Liu, S. Liu, B. Lorbeer, J. Lorkiewicz, H. H. Lu, F. Ludwig, K. Machau, W. Maciocha, C. Madec, C. Magueur, C. Maiano, I. Maksimova, K. Malcher, T. Maltezopoulos, E. Mamoshkina, B. Manschwetus, F. Marcellini, G. Marinkovic, T. Martinez, H. Martirosyan, W. Maschmann, M. Maslov, A. Mathiesen, U. Mavric, J. Meißner, K. Meissner, M. Messerschmidt, N. Meyners, G. Michalski, P. Michelato, N. Mildner, M. Moe, F. Moglia, C. Mohr, S. Mohr, W. Möller, M. Mommerz, L. Monaco, C. Montiel, M. Moretti, I. Morozov, P. Morozov, and D. Mross, A MHz-repetition-rate hard x-ray free-electron laser driven by a superconducting linear accelerator, *Nat. Photon.* **14**, 391 (2020).
- [19] S. Welker, M. Amin, and J. Küpper, CMInject: Python framework for the numerical simulation of nanoparticle injection pipelines (2021), submitted, arXiv:2102.05955 [physics].
- [20] S. Awel, R. A. Kirian, N. Eckerskorn, M. Wiedorn, D. A. Horke, A. V. Rode, J. Küpper, and H. N. Chapman, Visualizing aerosol-particle injection for diffractive-imaging experiments, *Opt. Exp.* **24**, 6507 (2016), arXiv:1512.06231 [physics].
- [21] L. Worbs, J. Lübke, N. Roth, A. K. Samanta, D. A. Horke, and J. Küpper, Light-sheet imaging for the recording of transverse absolute density distributions of gas-phase particle-beams from nanoparticle injectors, *Opt. Exp.* **27**, 36580 (2019), arXiv:1909.08922 [physics].
- [22] G. Schmid and U. Simon, Gold nanoparticles: assembly and electrical properties in 1–3 dimensions, *Chem. Commun.* , 697 (2005).
- [23] L. Dykman and N. Khlebtsov, Gold nanoparticles in biomedical applications: recent advances and perspectives, *Chem. Soc. Rev.* **41**, 2256 (2012).
- [24] Comsol, Multiphysics 5.5 (2019), cOMSOL Multiphysics v. 5.5. <http://www.comsol.com>. COMSOL AB, Stockholm, Sweden.
- [25] B. P. Marsh, N. Chada, R. R. Sanganna Gari, K. P. Sigdel, and G. M. King, The Hessian blob algorithm: Precise particle detection in atomic force microscopy imagery, *Sci. Rep.* **8**, 978 (2018).